• *Original Paper* •

# Northern Hemisphere Sudden Stratospheric Warming and Its Downward Impact in Four Chinese CMIP6 Models

Jian RAO[*1,2], Siming LIU[1,3], and Yuanhao CHEN[1]

[1]*Key Laboratory of Meteorological Disaster, Ministry of Education (KLME) / Joint International Research Laboratory of Climate and Environment Change (ILCEC) / Collaborative Innovation Center on Forecast and Evaluation of Meteorological Disasters (CIC-FEMD), Nanjing University of Information Science and Technology, Nanjing 210044, China*

[2]*Fredy and Nadine Herrmann Institute of Earth Sciences, The Hebrew University of Jerusalem, Edmond J. Safra Campus, Givat Ram Jerusalem 91904, Israel*

[3]*Department of the Geophysical Sciences, University of Chicago, Chicago 60637, USA*

## ABSTRACT

Using the World Meteorological Organization definition and a threshold-based classification technique, simulations of vortex displacement and split sudden stratospheric warmings (SSWs) are evaluated for four Chinese models (BCC-CSM2-MR, FGOALS-f3-L, FGOALS-g3, and NESM3) from phase 6 of the Coupled Model Intercomparison Project (CMIP6) with the Japanese 55-year reanalysis (JRA-55) as a baseline. Compared with six or seven SSWs in a decade in JRA-55, three models underestimate the SSW frequency by ~50%, while NESM3 doubles the SSW frequency. SSWs mainly appear in midwinter in JRA-55, but one-month climate drift is simulated in the models. The composite of splits is stronger than displacements in both the reanalysis and most models due to the longer pulse of positive eddy heat flux before onset of split SSWs. A wavenumber-1-like temperature anomaly pattern (cold Eurasia, warm North America) before onset of displacement SSWs is simulated, but cold anomalies are mainly confined to North America after displacement SSWs. Although the lower tropospheric temperature also displays a wavenumber-1-like pattern before split SSWs, most parts of Eurasia and North America are covered by cold anomalies after split SSWs in JRA-55. The models have different degrees of fidelity for the temperature anomaly pattern before split SSWs, but the wavenumber-2-like temperature anomaly pattern is well simulated after split SSWs. The center of the negative height anomalies in the Pacific sector before SSWs is sensitive to the SSW type in both JRA-55 and the models. A negative North Atlantic Oscillation is simulated after both types of SSWs in the models, although it is only observed for split SSWs.

**Key words:** sudden stratospheric warming, CMIP6, surface impact, model simulation

**Article Highlights:**

- A comparison of vortex displacement and split SSWs in four Chinese CMIP6 models (one from BCC, two from LASG, and one from NUIST) is reported.
- Models tend to underestimate the SSW frequency (except the model from NUIST) and simulate a one-month climate drift for SSWs.
- Tropospheric precursors and responses to displacement and split SSWs are simulated with different degrees of fidelity when compared with JRA-55.

---

## 1. Introduction

Sudden stratospheric warming (SSW) is one of the most radical phenomena in the climate system, which mainly occurs in the Northern Hemisphere midwinter (Andrews et al., 1987; Charlton and Polvani, 2007; Butler et al., 2015), with only two SSWs occurring in the Southern Hemisphere (September 2002 and 2020) in the satellite record (Newman and Nash, 2005; Rao et al., 2020d; Shen et al., 2020a, b). When SSWs appear, the Arctic stratosphere warms by tens of degrees within several days and the meridi-

———————————

\* Corresponding author: Jian RAO

  Email: raojian@nuist.edu.cn

onal temperature gradient in the subpolar region is reversed in the stratosphere. According to the sign of zonal-mean zonal winds at 10 hPa and 60°N, SSWs are further classified into major and minor events: major SSWs are additionally accompanied by a reversal of zonal winds from westerlies to easterlies, whereas minor SSWs only show a deceleration of westerlies without a direction reversal of zonal winds (Charlton and Polvani, 2007; Hu et al., 2014). On average, minor SSWs have a weaker strength and degree of stratosphere–troposphere coupling, so SSWs here refer to major events unless otherwise specified, although some minor SSWs are also accompanied by a clear downward propagation signal and exert strong influences on the lower-tropospheric climate (Wang and Chen, 2010; Rao et al., 2020d; Shen et al., 2020a, b).

Weakening, distortion, and displacement of the stratospheric polar vortex during major SSWs project onto a negative stratospheric annular mode, which propagates downward gradually in the following month(s) after onset of SSWs (Baldwin and Dunkerton, 1999; Baldwin et al., 2003; Cai and Ren, 2007; Sigmond et al., 2013). Therefore, stratospheric disturbance associated with SSWs is strongly coupled with the troposphere and serves as a potential source for tropospheric variability and predictability on the subseasonal time scale (e.g., Karpechko et al., 2018; Rao et al., 2018; Domeisen et al., 2020; Taguchi, 2020). For example, tropospheric and near-surface predictability is enhanced following SSWs (Sigmond et al., 2013; Tripathi et al., 2015, 2016). On average, a cold Eurasian continent–warm North American continent pattern is observed before SSWs at 850 hPa, while the two continents are anomalously cold after SSWs (Cao et al., 2019; Liu et al., 2019).

Based on the morphology of the stratospheric polar vortex, SSWs are classified into vortex displacement and vortex split events (Charlton and Polvani, 2007; Seviour et al., 2013; Liu et al., 2019; Rao et al., 2019). Early studies reported that the surface impact of displacement and split SSWs is similar (Charlton and Polvani, 2007; Mitchell et al., 2013), while other recent studies emphasize their differences (Nakagawa and Yamazaki, 2006; Seviour et al., 2016). Rao et al. (2020a) attribute the different impacts of displacement and split SSWs to their intensities, because on average the composite of displacement events is weaker than split events, although the methods and sample sizes might also cause a debate on whether impacts of the two SSW types are significantly different (Seviour et al., 2013, 2016; O'Callaghan et al., 2014).

Due to their important role in the climate system, a successful simulation of SSWs acts as an indispensable requisite when we score a model. For example, some models from phase 5 of the Coupled Model Intercomparison Project (CMIP5) can simulate several aspects of SSWs to different degrees of success based on single-model assessments [e.g., HadGEM2 in Osprey et al. (2013); CESM1-WACCM in Cao et al. (2019)] and multimodel studies [e.g., 21 models in Charlton-Perez et al. (2013); 13 high-top models in Seviour et al. (2016)]. Especially, Charlton-Perez et al.

(2013) suggest low-top models underestimate stratospheric variability on interannual and daily time scales. Osprey et al. (2013) compared the SSW frequency in the high-top and low-top configuration of their model and found a better reproduction of the SSW frequency in the high-top version than the low-top version. A suitable vertical resolution in the stratosphere is also necessary for models to capably simulate the stratospheric processes and stratosphere–troposphere coupling (Charlton-Perez et al., 2013; Osprey et al., 2013), although the high horizontal resolution is less important than the nice vertical resolution for models to simulate SSWs and the quasi-biennial oscillation (QBO) (Rao et al., 2020b, c).

Using a loose definition of SSWs and three criteria based on the leading mode of the extratropical zonal winds, Rao et al. (2015) found the CMIP5 multimodel ensemble, including four Chinese models (BCC-CSM1-1, BCC-CSM1-1-m, FGOALS-g2, and FGOALS-s2), underestimates the frequency of weak stratospheric polar vortex events. Such a bias is not exclusive to CMIP5 models, with it being also found in other models (Charlton et al., 2007; Mitchell et al., 2012; Ayarzagüena et al., 2013). However, we still know little about the performance of CMIP6 models in simulating SSWs. Recently, different CMIP6 modeling groups released their Diagnostic, Evaluation and Characterization of Klima (DECK) experiments (Kclima in Greek means "Climate"). One of the DECK experiments is a historical Atmospheric Model Intercomparison Project (AMIP) simulation from 1979–2014 (the other three are piControl, 4×CO2, and 1ptCO2) (Eyring et al., 2016). Our interest is not to include all of the CMIP6 models but to focus on four Chinese CMIP6 models that have been widely used in operations and/or some research projects in China (Zhou et al., 2020).

By using a strict WMO definition of SSWs and an available DECK experiment, this paper assesses the general performance of the four Chinese CMIP6 models in simulating SSWs, including their frequency, evolution, types, downward propagation, and surface impact. The paper is constructed as follows. Following the introduction, section 2 describes the models, experiments, and datasets. The SSW frequency and its seasonal distribution are compared in section 3. Evolutions and downward propagation of the stratospheric signals associated with SSWs follow in section 4. The tropospheric and near-surface responses to SSWs are shown in section 5. Finally, the main findings are summarized and discussed in section 6. It is expected that our assessments can help the four modeling groups locate the main biases of their models in the stratosphere, and thereby continue to improve these models in the future.

## 2.    Models, datasets and methods

### 2.1.    *Models, experiments and datasets*

Table 1 lists the four CMIP6 models with daily outputs available for AMIP experiments. The four models are BCC-

**Table 1**. The four Chinese CMIP6 models used in this study. One of the DECK experiments, AMIP, is commonly available for the four models. The size of the AMIP runs for each model is listed in the third column, and all ensemble members are analyzed in the composite. D/S in the fifth column represents the ratio of the vortex displacement and split SSWs. The CMIP6 AMIP experiments start from 1979 and end in 2014.

| Model | Full name (and affiliation) | Ensemble members | Resolution (and model top/levels around 100–10 hPa) | Total SSWs (and D/S) | Reference |
|---|---|---|---|---|---|
| BCC-CSM2-MR | Beijing Climate Center, Climate System Model version two, Medium Resolution (National Climate Center, China Meteorological Administration) | 3 | T106L46 (1.459 hPa / 18) | 9 + 13 + 8 (17/13 or 1.31) | Wu et al., 2019 |
| FGOALS-f3-L | Flexible Global Ocean–Atmosphere–Land System model, Finite-volume version 3, Low Resolution (State Key Laboratory of Numerical Modeling for Atmospheric Sciences and Geophysical Fluid Dynamics, Institute of Atmospheric Physics, Chinese Academy of Sciences) | 3 | C96L32 (2.16 hPa / 8) | 12 + 12 + 7 (11/20 or 0.55) | He et al., 2019 |
| FGOALS-g3 | Flexible Global Ocean–Atmosphere–Land System model, Grid-point version 3 (State Key Laboratory of Numerical Modeling for Atmospheric Sciences and Geophysical Fluid Dynamics, Institute of Atmospheric Physics, Chinese Academy of Sciences) | 5 | 180×80L26 (2.194 hPa / 7) | 7 + 12 + 6 + 12 + 10 (19/28 or 0.68) | Li et al., 2020 |
| NESM3 | Nanjing University of Information Science and Technology Earth System Model version 3 (Earth System Modeling Center, Nanjing University of Information Science and Technology) | 5 | T63L47 (1 hPa / 19) | 43 + 31 + 40 + 39 + 39 (116/76 or 1.53) | Cao et al., 2018 |

CSM2-MR, FGOALS-f3-L, FGOALS-g3, and NESM3, with their full name extensions and affiliations listed in the second column of Table 1. BCC-CSM2-MR is developed by the National Climate Center, China Meteorological Administration, and has a moderate horizontal resolution (T106, i.e., 320 × 160 grids, longitude × latitude). FGOALS-f3-L is developed by the State Key Laboratory of Numerical Modeling for Atmospheric Sciences and Geophysical Fluid Dynamics (LASG), Institute of Atmospheric Physics, Chinese Academy of Sciences, and has a moderate (although "L" denotes "low resolution") horizontal resolution (i.e., C96, i.e., 382 × 194 grids, longitude × latitude). FGOALS-g3 is also developed by LASG, but the atmospheric component is different and has a low horizontal resolution (i.e., 180 × 80 grids, longitude × latitude). NESM3 is developed by the Earth System Modeling Center, Nanjing University of Information Science and Technology, and has a low horizontal resolution (i.e., T63, 190 × 95 grids, longitude × latitude). For full details, readers are directed to the model descriptions (Cao et al., 2018; He et al., 2019; Wu et al., 2019; Li et al., 2020). All models have a model top around 1–2 hPa, incorporating the mid-to-lower stratosphere, where SSWs happen. In contrast, BCC-CSM2-MR and NESM3 (46 and 47 levels in total; 18 and 19 levels around 100–10 hPa) have a nicer vertical resolution than FGOALS-f3-L and FGOALS-g3 (32 and 26 levels in total; 8 and 7 levels around 100–10 hPa).

Because daily data from AMIP experiments were available for all of the four models at the beginning of this study (October 2019), we use the AMIP outputs. BCC-CSM2-MR and FGOALS-f3-L have three ensemble members, while FGOALS-g3 and NESM3 have five ensemble members (see the third column of Table 1). All the AMIP experiments are forced by the same external forcings, but the initial fields are different. All the ensemble members from the four Chinese CMIP6 models are used in our paper. Considering that the CMIP6 AMIP runs are from 1979–2014, the extracted Japanese 55-year Reanalysis (JRA-55) from 1979–2014 (JRA-55; Kobayashi et al., 2015) is used as a baseline for model evaluations. The SSW events from different reanalyses show little difference, especially during the satellite era since 1979 (Rao et al., 2015; Butler et al., 2017), so only the JRA-55 reanalysis is shown. Variables used in our paper include zonal and meridional winds, heights, and temperatures at pressure levels. Because NESM3 does not provide daily heights, we also calculate Ertel's potential vorticity (PV) as a substitute for height in the stratosphere.

## 2.2. Methods

There are many SSW definitions in the literature (Butler et al., 2015), which is not the focus of this study. Because the WMO definition is one of the most popular algorithms in the literature and considering that our results can be easily compared with earlier studies (Charlton et al., 2007; Butchart et al., 2011; Charlton-Perez et al., 2013; Hu et al., 2014; Manzini et al., 2014; Rao et al., 2018, 2020a), we still use this WMO SSW identification algorithm. According to the WMO SSW definition, the major SSW onset time is the first day when zonal-mean zonal winds at 10 hPa and

60°N reverse from westerlies to easterlies (Charlton and Polvani, 2007). The eddy heat flux ($\overline{v'T'}$) is proportional to the vertical component of the Eliassen–Palm (EP) flux ($F_z$), as a representation of the upward propagation of planetary waves (Limpasuvan et al., 2004; Polvani et al., 2017; Rao et al., 2018). The daily climatology is the long-term mean of each calendar day, and the daily climatology for each variable is smoothed with a 31-day running mean before being subtracted from the full field to get the anomaly field.

A vortex-centric diagnostic procedure developed by Seviour et al. (2013) is used to classify the SSW type. This method is established based on the geometry of the stratospheric polar vortex using the geopotential height or PV at 10 hPa. Two-dimensional vortex moments day by day are calculated in the procedure. Two parameters are required, including the centroid and aspect ratio of the stratospheric polar vortex represented by an equivalent ellipse (Mitchell et al., 2011; Seviour et al., 2016). Time series of the centroid and aspect ratio of the stratospheric polar vortex are calculated using a two-dimensional moment equation. The absolute and relative vortex moments (denoted by $M_{ab}$ and $J_{ab}$) of the modified PV (or height) field are extracted in the Cartesian coordinate. The latitude of the vortex centroid and the aspect ratio of polar vortex during each SSW event are saved using two-dimensional moment diagnostics and geopotential heights (or PVs) on isobaric levels (Matthewman et al., 2009). Note that the results from geopotential height and PV are highly correlated (Seviour et al., 2013, 2016).

Following Seviour et al. (2013, 2016), an SSW is classified into the vortex split group if the aspect ratio of the vortex is above 2.4 for at least seven days. An SSW is classified into the vortex displacement group if the centroid of the vortex is situated equatorward of 66°N for at least seven days. This threshold-based method has been confirmed to present a similar classification of split and displaced vortices as conventional methods (e.g., Charlton and Polvani, 2007; Mitchell et al., 2011). To show the feasibility of the threshold-based method, examples of vortex displacement and split SSWs are provided in Fig. 1 from JRA-55 and four CMIP6 models. Obviously, for displacement SSWs, the vortex is far biased from the North Pole, resembling a comma-like shape (Figs. 1a–e). In contrast, for split SSWs, the vortex breaks into two comparable pieces in models, as observed in the selected sample from the reanalysis (Figs. 1f–1j). Although the PV (value range: 30–50 PVU, −PV is drawn for an easy comparison with other models) is diagnosed for the vortex parameters in NESM3, the displacement and split are also clearly present as in other models.

## 3. How often do SSWs appear in CMIP6 models?

In the JRA-55 reanalysis, 23 SSWs appear during 1979–2014 (~0.64 events per year; Table 2). However, the models (excluding NESM3) tend to underestimate the SSW frequency: 30 events in 108 years for BCC-CSM2-MR (i.e.,
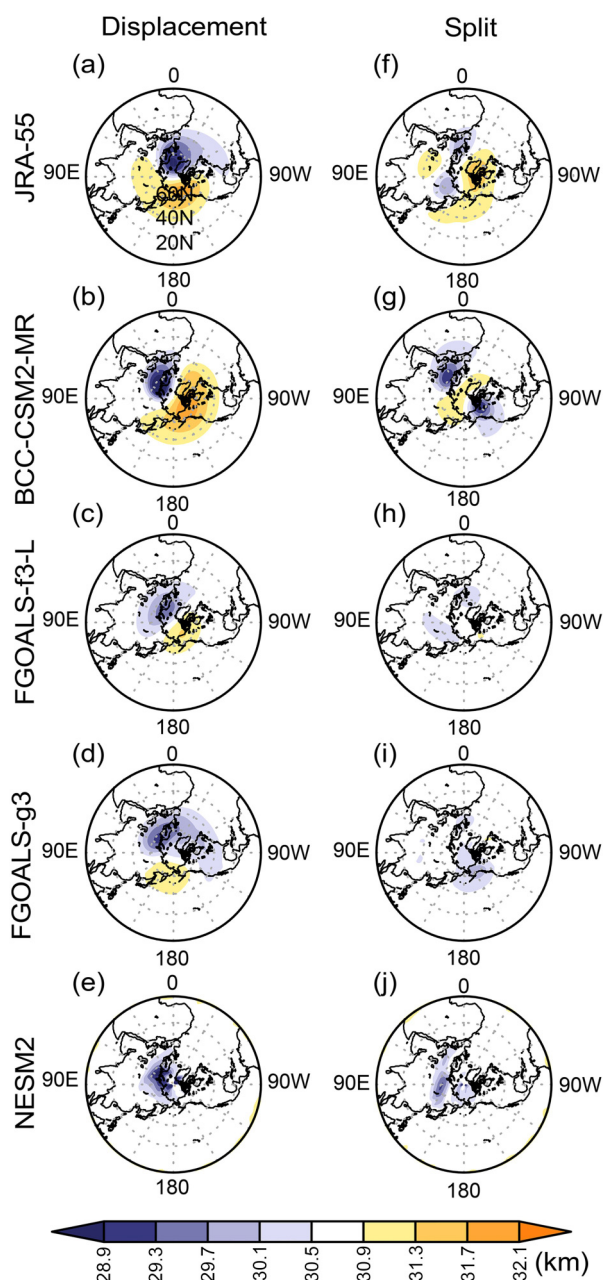


Fig. 1. Examples of the two types of SSWs for (a, f) JRA-55 on 16 February 1981 and 14 March 1988, (b, g) BCC-CSM2-MR on 11 March 2013 and 11 February 1982, (c, h) FGOALS-f3-L on 24 March 2013 and 10 March 2014, (d, i) FGOALS-g3 on 9 March 2014 and 28 February 1982, and (e, j) NESM3 on 13 February 1981 and 18 February 1980. The left-hand column shows the height or PV at 10 hPa for vortex displacement SSWs, and the right-hand column shows the height or PV at 10 hPa for the vortex split SSWs. All examples in the four Chinese CMIP6 models are selected from the first AMIP run. Note that daily heights are unavailable for NESM3 and Ertel's PVs is exclusively shown for this model (the PV sign is reversed for an easy comparison with other models; −PV value ranges: [−50, −30] PVU).

36 years from 1979–2014 in three AMIP runs; similar for other models), 31 events in 108 years for FGAOLS-f3-L, 47

events in 180 years for FGAOLS-g3, and 192 events in 180 years for NESM3 (see the fifth column of Table 1). The SSW frequency is 0.28, 0.29, 0.26, and 1.1 events per year for the four models, respectively. Namely, three models underestimate the SSW frequency by half, and NESM3 nearly doubles the observed SSW frequency. To get an overview of SSWs in the four CMIP6 models, the month-by-month distributions of SSWs are shown in Fig. 2. SSWs mainly occur

**Table 2.** Onset dates of SSW events and the corresponding type of the stratospheric polar vortex (D indicates a vortex displacement and S indicates a vortex split) in the JRA-55 reanalysis (1979–2014). The ratio of the vortex displacement and split SSWs is 1.3 (13/10) in JRA-55 during 1979–2014.

| SSW date | SSW type |
|---|---|
| 22 Feb 1979 | D |
| 29 Feb 1980 | D |
| 6 Feb 1981 | D |
| 4 Dec 1981 | D |
| 1 Jan 1985 | S |
| 23 Jan 1987 | D |
| 8 Dec 1987 | S |
| 14 Mar 1988 | S |
| 21 Feb 1989 | S |
| 15 Dec 1998 | D |
| 26 Feb 1999 | S |
| 20 Mar 2000 | D |
| 11 Feb 2001 | S |
| 31 Dec 2001 | D |
| 18 Jan 2003 | S |
| 5 Jan 2004 | D |
| 21 Jan 2006 | D |
| 24 Feb 2007 | D |
| 22 Feb 2008 | D |
| 24 Jan 2009 | S |
| 9 Feb 2010 | S |
| 24 Mar 2010 | D |
| 7 Jan 2013 | S |

in midwinter (January and February; unfilled bars in Fig. 1) in observations. Obviously, most models simulate a climate drift for SSWs, and more SSWs appear in late winter (February and March), and SSWs in NESM3 are nearly uniformly distributed in most wintertime months except February.

Seasonal distributions of vortex displacement and vortex split SSWs from November–March are shown in Fig. 3. As seen in Fig. 3a, vortex displacement SSWs are nearly uniformly distributed in December–February, followed by March. This peak in February is successfully simulated in NESM3, although SSWs occur much more frequently in this model than in JRA-55. Consistent with the distribution of SSWs in Fig. 2, all the other three models simulate much fewer displacement SSWs, and SSWs are drifted to late winter (February and/or March).

A stronger seasonality of split SSWs than displacement SSWs is observed for JRA-55, comparing the unfilled bars in Figs. 3a and b. More split SSWs appear in midwinter (January–February) in observations, and far fewer are observed in other wintertime months. Such a seasonality of SSWs observed in JRA-55 is drifted one month later
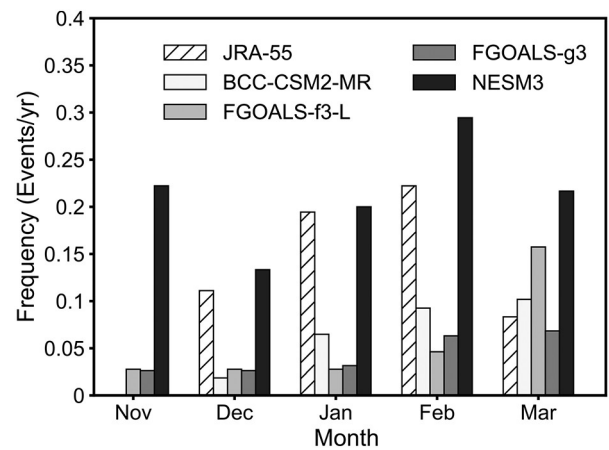


**Fig. 2.** Seasonal distribution of the total frequency of SSWs (units: number per year) from November to March for JRA-55 (hatched bars) and CMIP6 models (bars in gray shades).
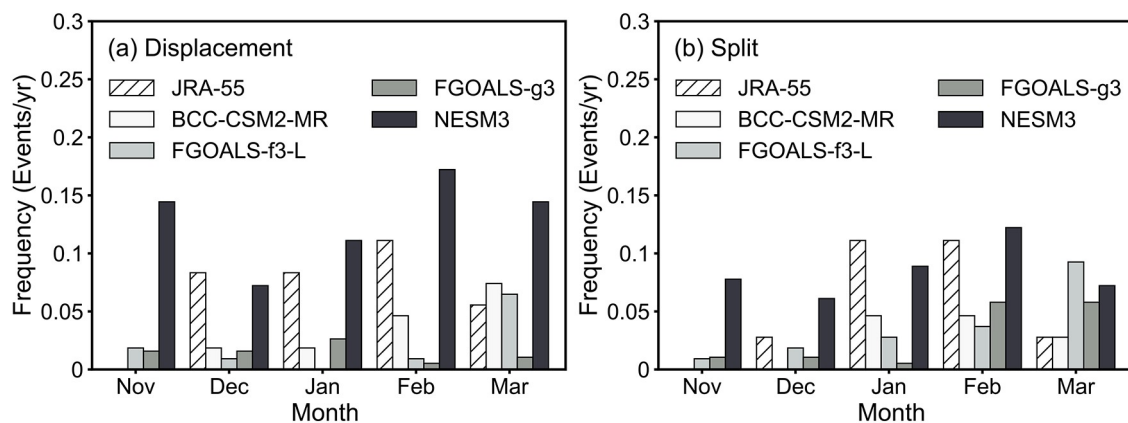


**Fig. 3.** Seasonal distribution of the frequency (units: events per year) of (a) vortex displacement SSWs and (b) vortex split SSWs in each wintertime month in the JRA-55 reanalysis during 1979–2014 and AMIP runs during 1979–2014 from four Chinese CMIP6 models.

to February–March for most models except BCC-CSM2-MR. Such a climate drift can be tracked to the seasonal evolution of the stratospheric polar vortex, which tends to get strongest in February (January) in models (reanalyses) [Fig. 5 in Rao et al. (2015)]. Compared with the three other models, BCC-CSM2-MR is the only one of the four Chinese CMIP6 models that simulates a stratospheric QBO (Rao et al., 2020b, c), which might also affect SSWs.

In addition to their contrasting seasonal distributions for both types of SSWs in JRA-55, the difference can also be identified for their intensities. We use the warming anomalies in the stratospheric polar cap to denote the intensity of SSWs. The composite strength of SSWs in each month for each type is shown in Fig. 4. To reverse the polar night jet that usually reaches climatological maxima in midwinter (Rao et al., 2015), the polar vortex anomalies are expected to be stronger for midwinter SSWs than events in November and March. This expectation is observed in JRA-55 (< 15 K in November and March versus > 20 K in midwinter) and simulated in almost all models for both displacement and split SSWs. Although the SSW frequency is not satisfactorily simulated by most models, the contrast in strength between displacement and split is simulated by models to different degrees of success. Specifically, on average, the strength of split SSWs is larger than displacement SSWs in JRA-55, which is simulated in some models (especially in BCC-CSM2-MR and NESM3).

## 4. Stratosphere–troposphere coupling during SSWs

During SSWs, the weak stratospheric polar vortex marks a phase of weak height (pressure) contrast between the midlatitudes and Arctic, which usually corresponds to a negative Northern Annular Mode (NAM) (Baldwin et al., 2003; Ren and Cai, 2007; Rao et al., 2020a). The negative NAM signals associated with SSWs propagate downward gradually with stratospheric anomalies leading tropospheric

anomalies and exhibit strong stratosphere–troposphere coupling. The composite temporal evolution of zonal-mean zonal wind anomalies over the extratropical latitude band (55°–75°N) is shown for two types of SSWs from the reanalysis and four models. As shown in the top row of Fig. 5, the easterly anomaly (or the westerly deceleration) develops more than a week before the onset date of SSWs, and the response of near-surface easterlies is most significant around day 20 for both displacement and split SSWs in JRA-55. The easterly anomaly in the stratosphere is stronger most of the time during day 0–60 for split SSWs than displacement in JRA-55 (maximum easterly anomaly magnitude: 25 versus 30 m s$^{-1}$; Figs. 5a, f and k).

The stronger stratospheric anomalies for split SSWs are simulated in three models (i.e., BCC-CSM2-MR, FGOALS-f3-L, and NESM3), consistent with the temperature anomalies in Fig. 4. It is easy to conclude that the split SSWs have a stronger impact on the troposphere than displacement SSWs, but Rao et al. (2020a) argue that the SSW strength is more important than the vortex morphology in inducing a low-level negative NAM response, which is beyond the scope of this study. It is also noticed that the composite intensity of displacement SSWs from FGOALS-g3 is stronger than split SSWs (maximum easterly anomaly magnitude: 20 versus 25 m s$^{-1}$; Figs. 5d, i and n). Although the composite difference between displacement and split SSWs is not significant most of the time after the SSW onset, the stronger easterlies for split SSWs are consistently simulated in the other three models (maximum easterly anomaly magnitude for displacement and split SSWs: 30 versus 35 m s$^{-1}$ for BCC-CSM2-MR, 15 versus 20 m s$^{-1}$ for FGOALS-f3-L, and 10 versus 15 m s$^{-1}$ for NESM3) as observed. The near-surface response due to the downward propagation of easterly anomalies is also simulated.

The evolutions of the polar cap temperature anomalies during SSWs are also compared for both SSW types in JRA-55 and the models (not shown). The temperature anomalies are observed to be larger for split SSWs than displace-
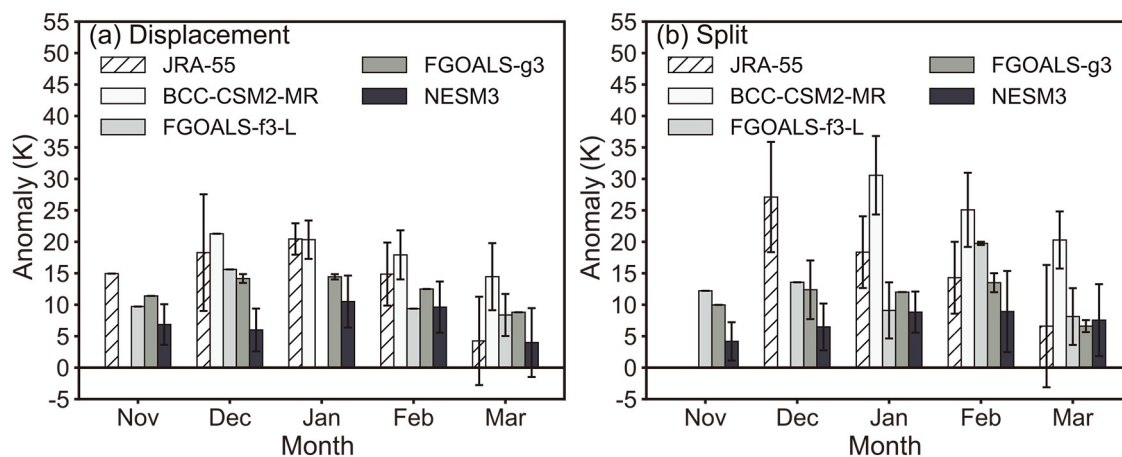


**Fig. 4**. Composite area-weighted polar (60°–90°N) temperature anomaly (units: K) at 10 hPa, ±5 days from the onset date of (a) vortex displacement SSWs and (b) vortex split SSWs in each wintertime month for the JRA-55 reanalysis and four Chinese CMIP6 models. The error bar shows uncertainty.
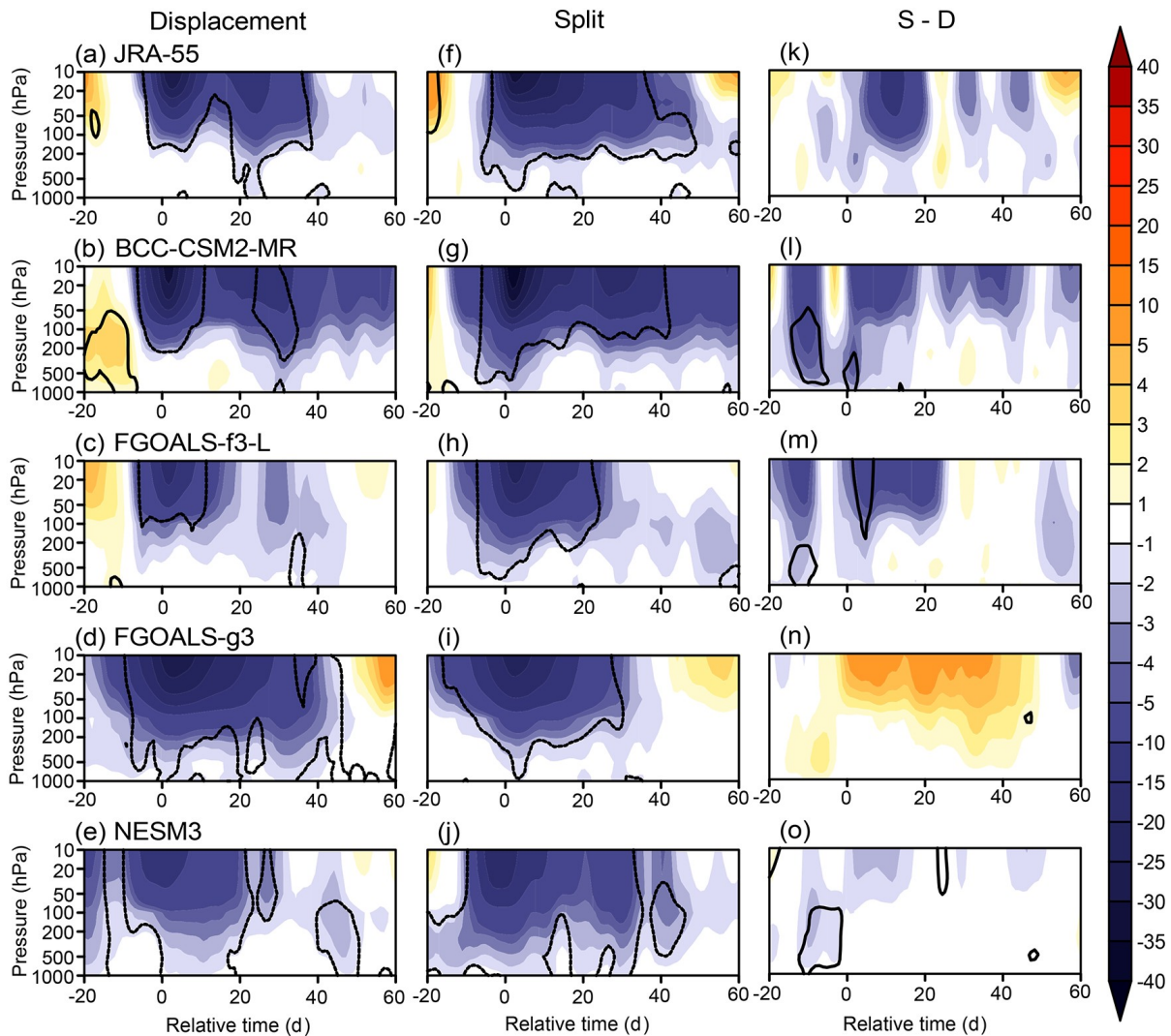
**Fig. 5**. Composite pressure–time evolution of the zonal mean zonal wind anomalies area-averaged over 55°–75°N (shading; units: m s⁻¹) from day −20 to day 60 relative to the onset date for (a–e) vortex displacement SSWs and (f–j) vortex split SSWs for (top row) the JRA-55 reanalysis during 1979–2014, and (second–last rows) four Chinese CMIP6 models during 1979–2014. The last column (k–o) shows the difference of vortex split minus displacement SSWs in each dataset. Black contours mark the composite zonal wind anomalies/differences at the 95% confidence level according to the Student's t-test.

ment SSWs in JRA-55 (maximum positive anomalies: ~8 versus ~10 K) and simulated to be so in BCC-CSM2-MR (~18 versus ~22 K), FGAOLS-f3-L (~8 versus ~10 K), and NESM3 (~6 versus ~7 K). Warm anomalies can propagate downward to the upper troposphere, but easterly anomalies can reach the near surface following onset of SSWs.

The stronger downward propagation and strength for split SSWs can be tracked to the stronger wave activities in the (upper) troposphere. As the eddy heat flux is proportional to the vertical component of EP flux, evolutions of eddy heat flux anomalies at 100 hPa in the 45°–75°N latitude band are shown in Fig. 6 for displacement and split SSWs, respectively. As seen from JRA-55 (green curves), although the total eddy heat flux anomalies for split SSWs are comparable to displacement SSWs from day −20 to day 0 (comparable maximum values: ~20 K m⁻¹; Figs. 6a and b), the eddy heat flux anomalies by the wavenumber-1 for

the vortex displacement SSWs are larger than those for the vortex split SSWs (maximum values: ~20 K versus ~15 K m s⁻¹, significantly different at the 95% confidence level). This means that within three weeks before onset of the vortex displacement SSWs, the upward propagation of planetary waves (especially wavenumber-1) strengthens (Figs. 6c and d). Similarly, the increase in the eddy heat flux by wavenumber-2 is larger for vortex split SSWs than for vortex displacement SSWs (maximum values: ~20 versus ~15 K m s⁻¹; Figs. 6e and f). After the onset of SSWs, the negative eddy heat flux anomalies develop. Namely, upward propagation of waves is prohibited after onset of SSWs due to the development of easterlies in the stratosphere. Compared with displacement SSWs, the longer time of eddy heat flux anomalies above zero (rather than the peak maxima) before day 0 in JRA-55 means more extra accumulation of energy in the stratospheric Arctic for split SSWs. This is successfully simu-
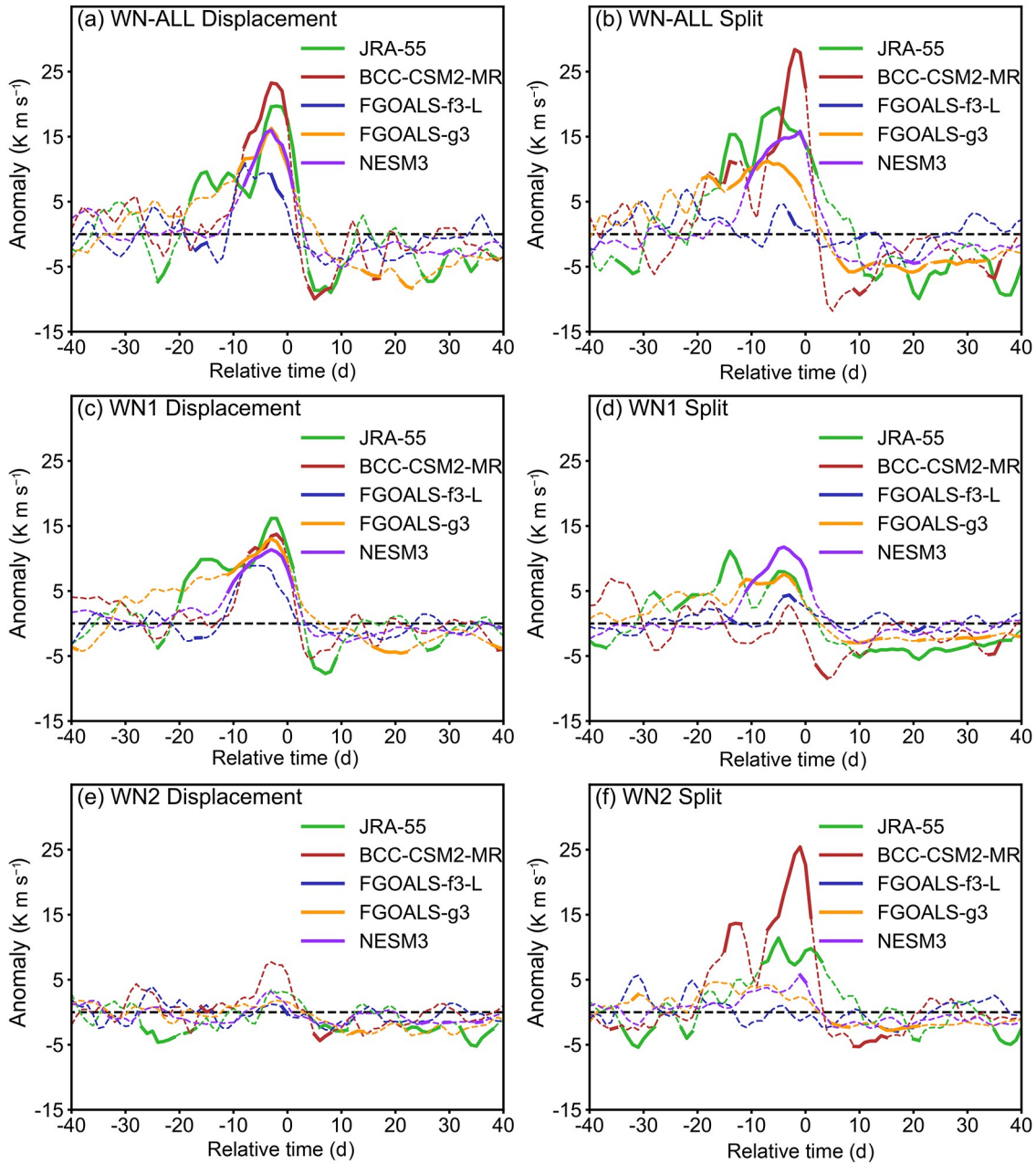
**Fig. 6**. Temporal evolution of eddy heat flux anomalies at 100 hPa area-averaged in the 45°–75°N latitude band (units: K m s$^{-1}$) from day −40 to day 40 with respect to the onset date of (left-hand column) vortex displacement SSWs and (right-hand column) vortex split SSWs from JRA-55 (green) and CMIP6 models (red, blue, orange, and purple). The top row shows the eddy heat by total waves, the middle row shows the wavenumber-1 components, and the bottom row shows the wavenumber-2 components. The thickened part of the dashed line denotes the composite at the 95% confidence level according to the *t*-test.

lated by BCC-CSM2-MR, FGAOLS-f3-L, and NESM3.

## 5.   **Impact of SSWs on the lower troposphere**

### 5.1.   *Lower-tropospheric temperature response to SSWs*

Previous studies have confirmed that the continental cold surge is modulated by extreme stratospheric events such as SSWs (Yu et al., 2018; Zhang et al., 2019). Compos-

ite temperature anomalies at 850 hPa for displacement SSWs are shown in Fig. 7 for JRA-55 and the models. In JRA-55, continental cold anomalies develop in North Eurasia before onset of SSWs from day −25 to day −5 (cold anomaly center magnitude: 3 K), and North America is covered with warm anomalies (warm anomaly center magnitude: 4 K). After the onset of displacement SSWs, cold anomalies decay in North Eurasia (cold anomaly center magnitude: 1.5 K), and cold anomalies develop in North Amer-
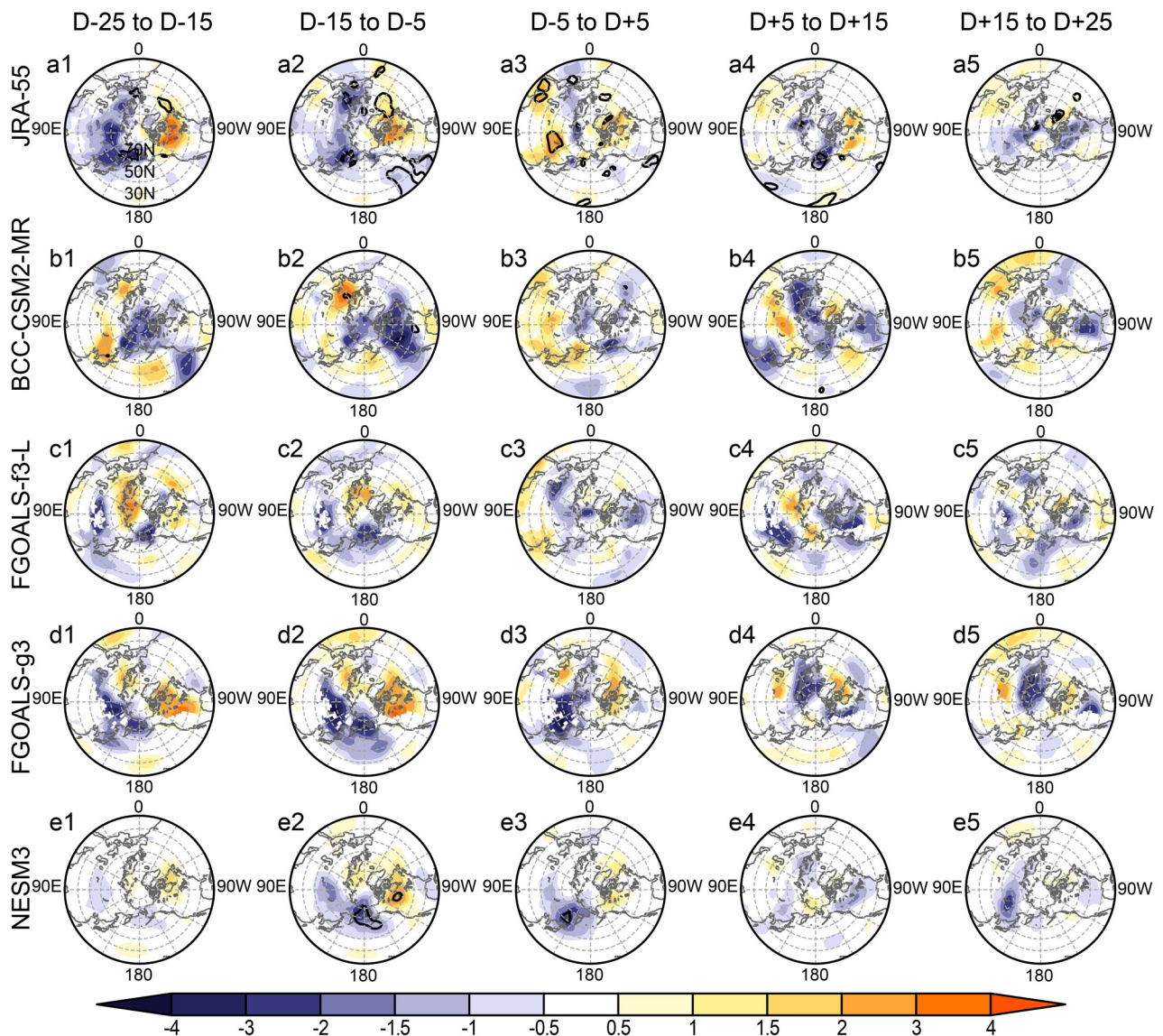
**Fig. 7**. (a) Composite temperature anomaly distribution (shading, units: K) at 850 hPa in (a) the JRA-55 reanalysis (1979–2014) and (b–e) four Chinese CMIP6 models (1979–2014) during day −25 to −15 (first column), day −15 to −5 (second column), day −5 to 5 (middle column), day 5 to 15 (fourth column), and day 15 to 25 (fifth column) relative to the onset date of vortex displacement SSWs. Black contours indicate that the composite temperature anomalies are significant at the 95% confidence level according to the *t*-test. The latitude range is 20°–90°N.

ica (cold anomaly center magnitude: 1.5 K; Fig. 7a). The four Chinese CMIP6 models simulate the evolution of the lower-tropospheric temperature response with different degrees of success (Figs. 7b–e). Specifically, BCC-CSM2-MR fails to reproduce the continental-scale cold anomalies in Eurasia before the onset of displacement SSWs, and North America is covered by large cold anomalies (albeit insignificant for most parts of the anomalies) in this model (Fig. 7b). In contrast, the other models generally simulate the cold Eurasian pattern before onset of displacement SSWs (Figs. 7c–e), although the temperature anomalies in FGOALS-f3-L and FGOALS-g3 are not as significant as in JRA-55 and NESM3 due to their different sample sizes. The cold North American pattern is also simulated by all of the

four models.

Similarly, Fig. 8 presents composite temperature anomalies at 850 hPa for split SSWs in JRA-55 and the models. A significant cold Eurasia (cold center anomaly magnitude: 4 K) and warm North America (warm center anomaly magnitude: 2–4 K) pattern is observed before onset of split SSWs in JRA55, whereas both continents are anomalously cold (3 versus 1.5 K) after onset of split SSWs (Fig. 8a). The temperature pattern before day 0 is not well simulated by BCC-CSM2-MR, but the uniform cold pattern in most parts of the Eurasian and North American continents (less significant than the observations) after day 0 (i.e., following onset of split SSWs) is successfully simulated (Fig. 8b). As for displacement SSWs, the other three models simulate the
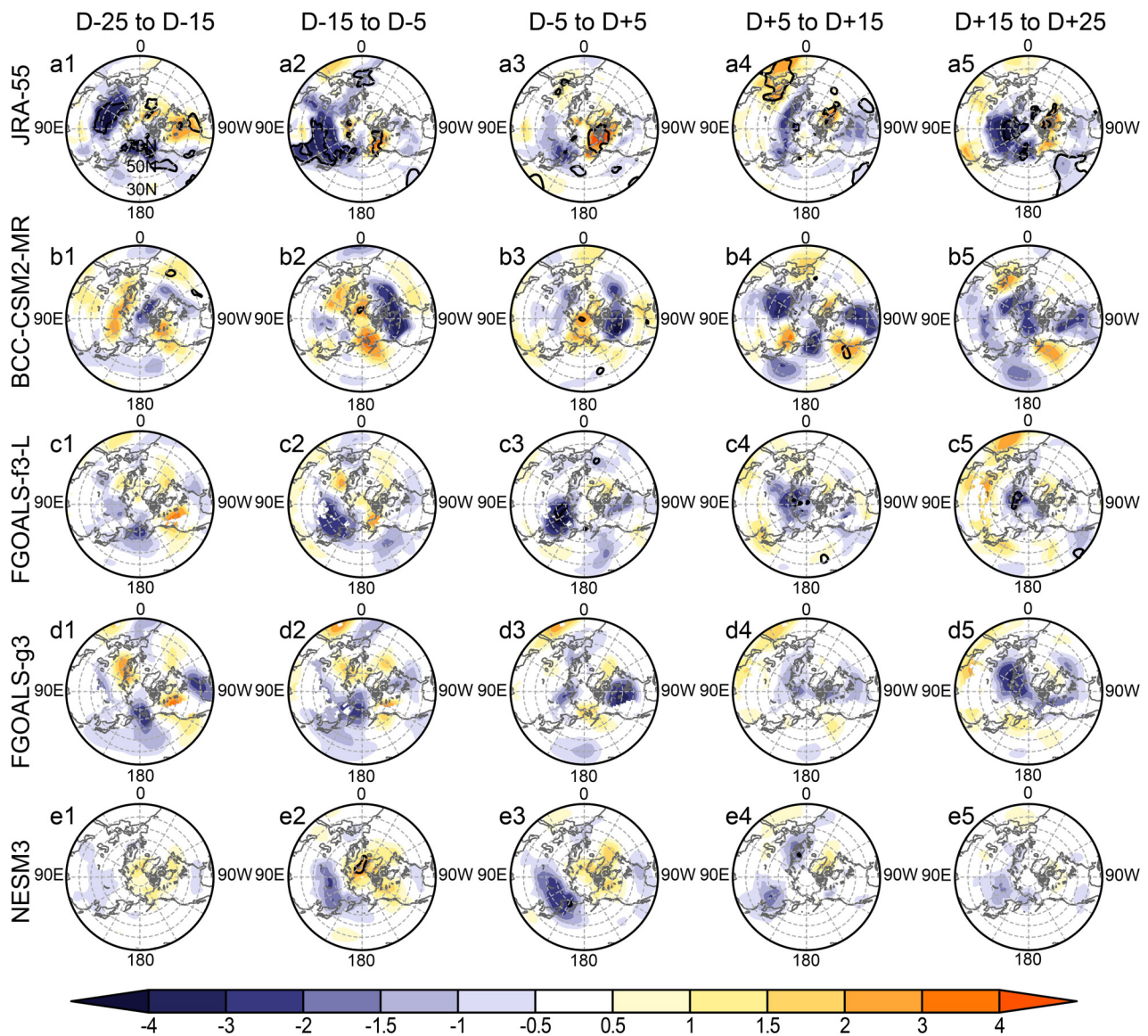
**Fig. 8**. (a) Composite temperature anomaly distribution (shading, units: K) at 850 hPa in (a) the JRA-55 reanalysis (1979–2014) and (b–e) four Chinese CMIP6 models (1979–2014) during day −25 to −15 (first column), day −15 to −5 (second column), day −5 to 5 (middle column), day 5 to 15 (fourth column), and day 15 to 25 (fifth column) relative to the onset date of vortex split SSWs. Black contours indicate that the composite temperature anomalies are significant at the 95% confidence level according to the *t*-test. The latitude range is 20°–90°N.

cold signals in most parts of Eurasia before and around the onset date of split SSWs, albeit with a low significance level (Figs. 8b–e). However, the cold anomalies after split SSWs in most parts of North America are underestimated.

Comparing displacement and split SSWs, the cold patterns after the onset date are different. For displacement SSWs, cold anomalies mainly develop in North America, and the cold anomalies in Eurasia decay, more resembling a wavenumber-1 pattern. For split SSWs, most parts of both the Eurasian and North American continents are covered with cold anomalies, more resembling a wavenumber-2 pattern. Liu et al. (2019) evaluated two high-top models (CESM1-WACCM and CESM2-WACCM) from CMIP5/6, and the simulated low-tropospheric response was similar to

that in other CMIP5/6 models (Seviour et al., 2016; Cao et al., 2019; Liu et al., 2019). In short, the surface response to SSWs is more consistently captured by models than the SSW frequency.

### 5.2. *Tropospheric circulation response to SSWs*

On the one hand, tropospheric wave activities can force the development of SSWs; and on the other hand, SSWs can impact the troposphere after onset by inducing a NAM-like response from the stratosphere to the troposphere (i.e., easterly anomalies in the circumpolar region, Fig. 5; or positive polar cap height anomalies; not shown). The two-way coupling is dominated by different processes before and after onset of SSWs. To test the variation of the tropospheric circu-
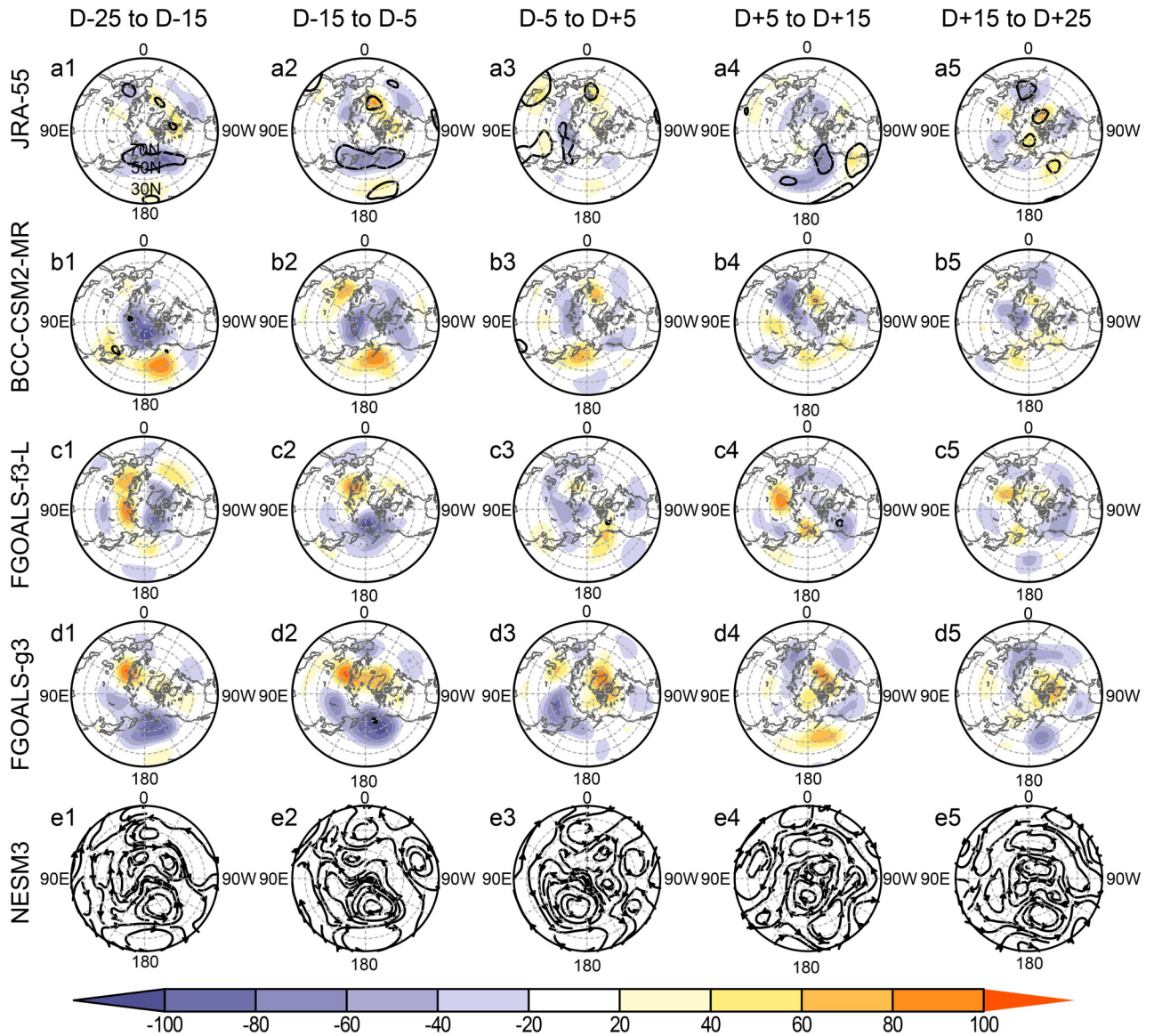
**Fig. 9**. Composite geopotential height anomalies (shading; units: gpm) at 500 hPa in (a) the JRA-55 reanalysis (1979–2014) and (b–d) three CMIP6 models (BCC-CSM2-MR, FGAOLS-f3-L, and FGOALS-g3) during day −25 to −15 (first column), day −15 to −5 (second column), day −5 to 5 (middle column), day 5 to 15 (fourth column), and day 15 to 25 (fifth column) relative to the onset date of vortex displacement SSWs. Black contours indicate that the composite height anomalies are significant at the 95% confidence level according to the *t*-test. (e) Composite wind anomalies at 500 hPa for NESM3 due to the unavailability of heights. The latitude range is 20°–90°N. Note that daily heights are unavailable for NESM3 and streamlines are exclusively shown for this model.

lation, Fig. 9 shows the evolution of height anomalies at 500 hPa in JRA-55 and models during displacement SSWs. As seen from JRA-55, a significant low anomaly center develops over the North Pacific from day −25 to day −5, and a significant high anomaly center forms in the subtropical central Pacific in observations (Fig. 9a). Such a height anomaly distribution resembles a positive phase of the Pacific–North American (PNA) pattern, with another positive lobe in North Canada and another negative lobe in the eastern U.S., respectively. The negative height anomalies over the North Pacific extend westward to the coastal region of China, which can be projected onto the negative phase of the west-

ern Pacific (WP) pattern (Wallace and Gutzler, 1981). The low anomaly center over the North Pacific has been reported as a precursor of a (following) weakening stratospheric polar vortex on both subseasonal and interannual time scales (Garfinkel et al., 2010; Dai and Tan, 2016; Hu et al., 2017; Rao et al., 2019). Around and after onset of SSWs, the tropospheric circulation anomalies decay and no significant circulation systems are observed (Fig. 9a).

The models simulate the tropospheric circulation anomaly pattern with different degrees of fidelity. The negative height anomaly center over the North Pacific in observations is biased to the Arctic in BCC-CSM2-MR from day
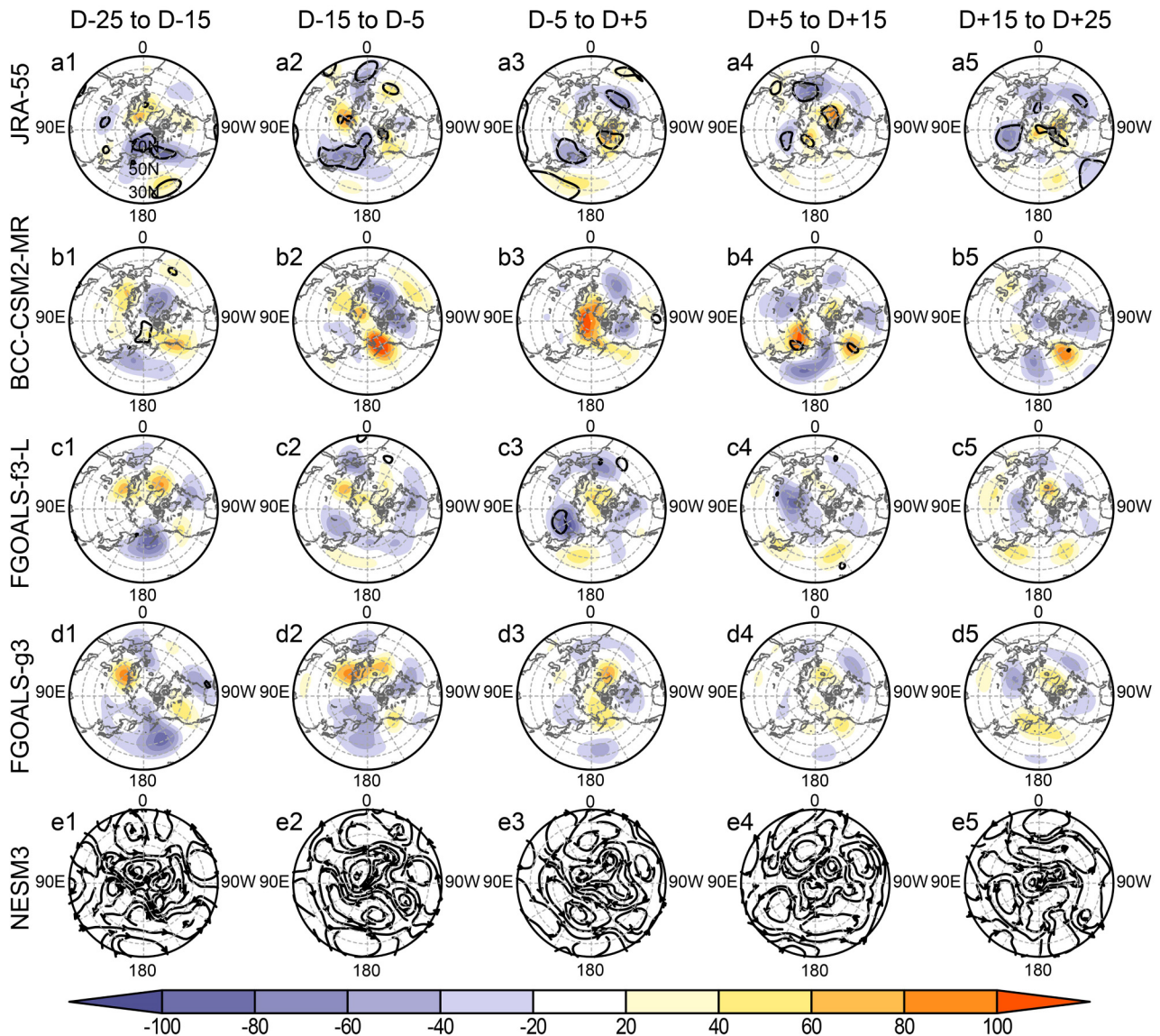
**Fig. 10**. Composite geopotential height anomalies (shading; units: gpm) at 500 hPa in (a) the JRA-55 reanalysis (1979–2014) and (b–d) three CMIP6 models (BCC-CSM2-MR, FGAOLS-f3-L, and FGOALS-g3) during day −25 to −15 (first column), day −15 to −5 (second column), day −5 to 5 (middle column), day 5 to 15 (fourth column), and day 15 to 25 (fifth column) relative to the onset date of vortex split SSWs. Black contours indicate that the composite height anomalies are significant at the 95% confidence level according to the *t*-test. (e) Composite wind anomalies at 500 hPa for NESM3 due to the unavailability of heights. The latitude range is 20°–90°N. Note that daily heights are unavailable for NESM3 and streamlines are exclusively shown for this model.

−25 to day −5, and the high anomaly center over the subtropical central Pacific is located further poleward (Fig. 9b). In contrast, the negative height anomaly (i.e., the cyclone anomaly) center over the North Pacific before SSWs is well simulated in the other models (Figs. 9c–e). As the tropospheric wave perturbation propagates upward (denoted by the large eddy heat flux pulse in Fig. 6a), the precursor decays and the low center moves westward to North Asia during day −5 to day 5 in JRA-55 and the models (middle column in Fig. 9). Although the height dipole (a high center over Iceland and a low center in the subtropics) in the Atlantic sector is not clearly observed in JRA-55, it is consistently simulated in the four CMIP6 models from day 15 to day 25, resembling

the negative phase of the North Atlantic Oscillation (NAO).

Similarly, the evolution of height anomalies at 500 hPa in JRA-55 and the models during vortex split SSWs is shown in Fig. 10. Different from the observed tropospheric height pattern associated with displacement SSWs, the negative height anomaly center is situated further west from the Aleutian Islands, more resembling a WP pattern most of the time from day −25 to day 5 in JRA-55 (Fig. 10a). The circulation anomalies in the Pacific sector gradually decay after onset of SSWs, and a strong NAO is observed after onset of SSWs in observations.

Models have different skills in simulating tropospheric circulation evolutions during SSWs. The low center devel-

ops only during day −25 to day −15 in BCC-CSM2-MR (Fig. 10b), but decays faster than in JRA-55 and other models. A negative NAO is not clearly simulated after onset of SSWs for this model. In contrast, the WP-like pattern during day −25 to day 5 is well captured by FGAOLS-f3-L, FGOALS-g3, and NESM3 (Figs. 10c–e). Models tend to underestimate the post-SSW tropospheric response amplitude in the Atlantic sector.

## 6. Summary and discussion

SSW is one of the most radical phenomena in the stratosphere–troposphere coupling system, and its successful simulation is a basic requisite for models emphasizing the role of the stratosphere. Based on a strict WMO SSW definition and a threshold-classification criterion, this paper studies the different statistical characteristics and impacts of vortex displacement and split SSWs. Several aspects are assessed for four Chinese CMIP6 models with daily AMIP outputs available. The main findings are as follows.

In observations (represented by JRA-55), six or seven SSWs happen in 10 years (0.64 events per year). BCC-CSM2-MR, FGOALS-f3-L, and FGOALS-g3 underestimate the SSW frequency nearly by half, while NESM3 doubles the SSW frequency. In addition, most SSWs appear in midwinter (January and February), but one-month climate drift for SSWs is consistently simulated in models (SSWs mainly appear in February and March).

As shown in observations, displacement SSWs are nearly evenly distributed in December–March, while split SSWs primarily happen in January and February, determining the seasonal distribution of total SSWs. Both displacement and split SSWs tend to appear in late winter in models, so models cannot capture the seasonality of split (and therefore total) SSWs.

On average, the composite strength of split SSWs is larger than that of displacement SSWs in both the reanalysis and most models, although it does not mean that a split SSW is necessarily stronger than a displacement SSW. The longer pulse of strong positive eddy heat flux before onset of split SSWs explains the stronger stratospheric signals than displacement SSWs for reanalysis and most models. An exception is that the composite of displacement SSWs is stronger than the composite of split SSWs in FGAOLS-g3, although the cause for such a bias is still unknown.

Displacement SSWs and split SSWs have different impacts on lower troposphere (or the near surface), and the air temperature pattern is also different before and after the onset of SSWs. Before onset of displacement SSWs, cold anomalies cover North Eurasia and warm anomalies cover Arctic Canada in observations. After that, cold anomalies in North Eurasia gradually decay and the cold anomalies are confined to North America. Such a wavenumber-1-like temperature anomaly pattern (cold Eurasia and warm North America) in the Northern Hemisphere before onset of displacement SSWs are well forecasted by FGOALS-f3-L,

FGOALS-g3, and NESM3 (the skill in BCC-CSM2-MR is relatively low). The cold anomalies in North America after onset of displacement SSWs are captured by all models.

Similarly, warm anomalies also form in Arctic Canada before onset of split SSWs, but most parts of the two continents after onset of split SSWs are covered by cold anomalies in midlatitudes as seen from JRA-55. The models have different degrees of fidelity for the temperature anomaly pattern before onset of split SSWs, but the two cold continents are captured by all the models. The two cold continents after onset of split SSWs generally display a wavenumber-2-like temperature anomaly pattern in both the reanalysis and models.

The tropospheric circulation precursors are different for both types of SSWs in observations. Before displacement SSWs, the North Pacific height anomalies are situated near the Aleutian Islands and the PNA pattern develops to its positive phase in JRA-55. However, before split SSWs, the negative height anomalies in the Pacific sector move westward to the coast of East Asia, and the WP pattern develops to its negative phase. The center of the negative height anomalies in the Pacific sector before onset of SSWs is also sensitive to the SSW type in the models. In observations, a negative NAO is observed only after split SSWs, but it is simulated after both types of SSWs in the models, with the response amplitude underestimated.

To summarize, many aspects of SSWs can be well simulated by Chinese CMIP6 models, although some biases also exist. Rao et al. (2015) used a loose SSW definition and still found that far fewer SSWs were simulated in CMIP5 models. In addition, it is also noted that the CMIP6 models (i.e., BCC-CSM2-MR, FGOALS-f3-L, and FGOALS-g3) simulate more SSWs than their CMIP5 versions (i.e., BCC-CSM1-1, FGOALS-s2, and FGOALS-g2) (2–3 versus 1–2 SSWs per decade). A comparison of SSW simulation between CMIP5 and CMIP6 models is left for a future study. It is also noted that the significance levels in the models are relatively lower than in the reanalysis, although their composite patterns are very similar. This relatively low significance level is mainly attributed to a small sample size of SSWs in the models due to their underestimation of the SSW frequency and the deficiency of the model's configuration and coarse (vertical) resolution in capturing the characteristics of the SSW (Charlton-Perez et al., 2013; Osprey et al., 2013; Cai et al., 2017; Rao et al., 2020b, c). Comparing with some previous studies (Cao et al., 2019; Liu et al., 2019), high-top models with a finer vertical resolution in the stratosphere (e.g., CESM1-WACCM, CESM2-WACCM) tend to simulate more SSWs. In our four Chinese CMIP6 models, the atmospheric top is around 1 or 2 hPa, so the middle and lower stratosphere is included in those coupled models. In contrast, it is also found that NESM3 has the highest top of the four models, which stops around 1 hPa. Actually, NESM3 also simulates the most SSWs out of the four models.

Although the SSW frequency is underestimated in three

models, the tropospheric precursors for SSWs are realistically simulated by most models, reflecting a better capture of bottom-up effect in models. The bias in the top-down effect of the stratospheric variability related to the SSW in low-top models might explain the deficiency in the simulation of the near-surface Arctic Oscillation pattern and East Asian winter climate (e.g., Wei et al., 2018; Gong et al., 2019), although the four models have a good simulation in some aspects of the tropospheric variability, including monsoon systems, Madden–Julian Oscillation, rainfall and typhoons (He et al., 2019; Li et al., 2020). However, SSWs are forced by different sources: some are caused by lower-tropospheric perturbation, while more are related to lower-stratospheric wave activities (de la Cámara et al., 2019; White et al., 2019). More efforts are still required for the modeling developers to improve several aspects of those models, including a higher model top to incorporate the whole stratosphere and even the mesosphere, a complete gravity wave parameterization from different sources, a chemical feedback to the stratosphere by adding a chemistry module, and improvements in other model components (e.g., ocean, land, and ice) to produce a better stratospheric response to boundary variations.

# REFERENCES

Andrews, D. G., J. R. Holton, and C. B. Leovy, 1987: *Middle Atmosphere Dynamics*. Academic Press, 491 pp.

Ayarzagüena, B., U. Langematz, S. Meul, S. Oberländer, J. Abalichin, and A. Kubin, 2013: The role of climate change and ozone recovery for the future timing of major stratospheric warmings. *Geophys. Res. Lett.*, **40**(10), 2460–2465, https://doi.org/10.1002/grl.50477.

Baldwin, M. P., and T. J. Dunkerton, 1999: Propagation of the Arctic Oscillation from the stratosphere to the troposphere. *J. Geophys. Res.*, **104**(D24), 30937–30946, https://doi.org/10.1029/1999jd900445.

Baldwin, M. P., D. B. Stephenson, D. W. J. Thompson, T. J. Dunkerton, A. J. Charlton, and A. O'Neill, 2003: Stratospheric memory and skill of extended-range weather forecasts. *Science*, **301**(5633), 636–640, https://doi.org/10.1126/science.1087143.

Butchart, N., and Coauthors, 2011: Multimodel climate and variability of the stratosphere. *J. Geophys. Res.*, **116**(D5), D05102, https://doi.org/10.1029/2010jd014995.

Butler, A. H., D. J. Seidel, S. C. Hardiman, N. Butchart, T. Birner, and A. Match, 2015: Defining sudden stratospheric warmings. *Bull. Amer. Meteor. Soc.*, **96**(11), 1913–1928, https://doi.org/10.1175/bams-d-13-00173.1.

Butler, A. H., J. P. Sjoberg, D. J. Seidel, and K. H. Rosenlof, 2017: A sudden stratospheric warming compendium. *Earth System Science Data*, **9**(1), 63–76, https://doi.org/10.5194/essd-9-63-2017.

Cai, M., and R. C. Ren, 2007: Meridional and downward propagation of atmospheric circulation anomalies. Part I: Northern Hemisphere cold season variability. *J. Atmos. Sci.*, **64**(6), 1880–1901, https://doi.org/10.1175/jas3922.1.

Cai, Z. L., K. Wei, L. Y. Xu, X. Q. Lan, W. Chen, and D. Nath, 2017: The influences of the model configuration on the simulation of stratospheric Northern-Hemisphere polar vortex in the CMIP5 models. *Advances in Meteorology*, **2017**, 7326759, https://doi.org/10.1155/2017/7326759.

Cao, C., Y. H. Chen, J. Rao, S. M. Liu, S. Y. Li, M. H. Ma, and Y. B. Wang, 2019: Statistical characteristics of major sudden stratospheric warming events in CESM1-WACCM: A comparison with the JRA55 and NCEP/NCAR reanalyses. *Atmosphere*, **10**(9), 519, https://doi.org/10.3390/atmos10090519.

Cao, J., and Coauthors, 2018: The NUIST Earth System Model (NESM) version 3: Description and preliminary evaluation. *Geoscientific Model Development*, **11**(7), 2975–2993, https://doi.org/10.5194/gmd-11-2975-2018.

Charlton, A. J., and L. M. Polvani, 2007: A new look at stratospheric sudden warmings. Part I: Climatology and modeling benchmarks. *J. Climate*, **20**(3), 449–469, https://doi.org/10.1175/jcli3996.1.

Charlton, A. J., and Coauthors, 2007: A new look at stratospheric sudden warmings. Part II: Evaluation of numerical model simulations. *J. Climate*, **20**(3), 470–488, https://doi.org/10.1175/jcli3994.1.

Charlton-Perez, A. J., and Coauthors, 2013: On the lack of stratospheric dynamical variability in low-top versions of the CMIP5 models. *J. Geophys. Res.*, **118**(6), 2494–2505, https://doi.org/10.1002/jgrd.50125.

Dai, Y., and B. K. Tan, 2016: The western Pacific pattern precursor of major stratospheric sudden warmings and the ENSO modulation. *Environmental Research Letters*, **11**(12), 124032, https://doi.org/10.1088/1748-9326/aa538a.

de la Cámara, A., T. Birner, and J. R. Albers, 2019: Are sudden stratospheric warmings preceded by anomalous tropospheric wave activity? *J. Climate*, **32**(21), 7173–7189, https://doi.org/10.1175/jcli-d-19-0269.1.

Domeisen, D. I. V., and Coauthors, 2020: The role of the stratosphere in subseasonal to seasonal prediction: 2. Predictability arising from stratosphere-troposphere coupling. *J. Geophys. Res.*, **125**(2), e2019jd030923, https://doi.org/10.1029/2019jd030923.

Eyring, V., S. Bony, G. A. Meehl, C. A. Senior, B. Stevens, R. J. Stouffer, and K. E. Taylor, 2016: Overview of the Coupled Model Intercomparison Project Phase 6 (CMIP6) experimental design and organization. *Geoscientific Model Development*, **9**(5), 1937–1958, https://doi.org/10.5194/gmd-9-1937-2016.

Garfinkel, C. I., D. L. Hartmann, and F. Sassi, 2010: Tropospheric precursors of anomalous Northern Hemisphere strato-

spheric polar vortices. *J. Climate*, **23**(12), 3282−3299, https://doi.org/10.1175/2010jcli3010.1.

Gong, H. N., L. Wang, W. Chen, R. G. Wu, W. Zhou, L. Liu, D. Nath, and X. Q. Lan, 2019: Diversity of the wintertime Arctic Oscillation pattern among CMIP5 models: Role of the stratospheric polar vortex. *J. Climate*, **32**(16), 5235−5250, https://doi.org/10.1175/jcli-d-18-0603.1.

He, B., and Coauthors, 2019: CAS FGOALS-f3-L model datasets for CMIP6 historical atmospheric model intercomparison project simulation. *Adv. Atmos. Sci.*, **36**(8), 771−778, https://doi.org/10.1007/s00376-019-9027-8.

Hu, J. G., R. C. Ren, and H. M. Xu, 2014: Occurrence of winter stratospheric sudden warming events and the seasonal timing of spring stratospheric final warming. *J. Atmos. Sci.*, **71**(7), 2319−2334, https://doi.org/10.1175/jas-d-13-0349.1.

Hu, J. G., T. Li, H. M. Xu, and S. Y. Yang, 2017: Lessened response of boreal winter stratospheric polar vortex to El Niño in recent decades. *Climate Dyn.*, **49**(1−2), 263−278, https://doi.org/10.1007/s00382-016-3340-z.

Karpechko, A. Y., A. Charlton-Perez, M. Balmaseda, N. Tyrrell, and F. Vitart, 2018: Predicting sudden stratospheric warming 2018 and its climate impacts with a multimodel ensemble. *Geophys. Res. Lett.*, **45**(24), 13538−13546, https://doi.org/10.1029/2018gl081091.

Kobayashi, S., and Coauthors, 2015: The JRA-55 reanalysis: General specifications and basic characteristics. *J. Meteor. Soc. Japan*, **93**(1), 5−48, https://doi.org/10.2151/jmsj.2015-001.

Li, L. J., and Coauthors, 2020: The GAMIL3: Model description and evaluation. *J. Geophys. Res.*, **125**(15), e2020jd032574, https://doi.org/10.1029/2020jd032574.

Limpasuvan, V., D. W. J. Thompson, and D. L. Hartmann, 2004: The life cycle of the Northern Hemisphere sudden stratospheric warmings. *J. Climate*, **17**(13), 2584−2596, https://doi.org/10.1175/1520-0442(2004)017<2584:tlcotn>2.0.co;2.

Liu, S. M., Y. H. Chen, J. Rao, C. Cao, S. Y. Li, M. H. Ma, and Y. B. Wang, 2019: Parallel comparison of major sudden stratospheric warming events in CESM1-WACCM and CESM2-WACCM. *Atmosphere*, **10**(11), 679, https://doi.org/10.3390/atmos10110679.

Manzini, E., and Coauthors, 2014: Northern winter climate change: Assessment of uncertainty in CMIP5 projections related to stratosphere-troposphere coupling. *J. Geophys. Res.*, **119**(13), 7979−7998, https://doi.org/10.1002/2013jd021403.

Matthewman, N. J., J. G. Esler, A. J. Charlton-Perez, and L. M. Polvani, 2009: A new look at stratospheric sudden warmings. Part III: Polar vortex evolution and vertical structure. *J. Climate*, **22**(6), 1566−1585, https://doi.org/10.1175/2008jcli2365.1.

Mitchell, D. M., A. J. Charlton-Perez, and L. J. Gray, 2011: Characterizing the variability and extremes of the stratospheric polar vortices using 2D moment analysis. *J. Atmos. Sci.*, **68**(6), 1194−1213, https://doi.org/10.1175/2010jas3555.1.

Mitchell, D. M., and Coauthors, 2012: The nature of Arctic polar vortices in chemistry-climate models. *Quart. J. Roy. Meteor. Soc.*, **138**(668), 1681−1691, https://doi.org/10.1002/qj.1909.

Mitchell, D. M., L. J. Gray, J. Anstey, M. P. Baldwin, and A. J. Charlton-Perez, 2013: The influence of stratospheric vortex displacements and splits on surface climate. *J. Climate*,

**26**(8), 2668−2682, https://doi.org/10.1175/jcli-d-12-00030.1.

Nakagawa, K. I., and K. Yamazaki, 2006: What kind of stratospheric sudden warming propagates to the troposphere? *Geophys. Res. Lett.*, **33**(4), L04801, https://doi.org/10.1029/2005gl024784.

Newman, P. A., and E. R. Nash, 2005: The unusual Southern Hemisphere stratosphere winter of 2002. *J. Atmos. Sci.*, **62**(3), 614−628, https://doi.org/10.1175/jas-3323.1.

O'Callaghan, A., M. Joshi, D. Stevens, and D. Mitchell, 2014: The effects of different sudden stratospheric warming types on the ocean. *Geophys. Res. Lett.*, **41**(21), 7739−7745, https://doi.org/10.1002/2014gl062179.

Osprey, S. M., L. J. Gray, S. C. Hardiman, N. Butchart, and T. J. Hinton, 2013: Stratospheric variability in twentieth-century CMIP5 simulations of the Met Office climate model: High top versus low top. *J. Climate*, **26**(5), 1595−1606, https://doi.org/10.1175/jcli-d-12-00147.1.

Polvani, L. M., L. T. Sun, A. H. Butler, J. H. Richter, and C. Deser, 2017: Distinguishing stratospheric sudden warmings from ENSO as key drivers of wintertime climate variability over the North Atlantic and Eurasia. *J. Climate*, **30**(6), 1959−1969, https://doi.org/10.1175/jcli-d-16-0277.1.

Rao, J., R. C. Ren, and Y. Yang, 2015: Parallel comparison of the northern winter stratospheric circulation in reanalysis and in CMIP5 models. *Adv. Atmos. Sci.*, **32**(7), 952−966, https://doi.org/10.1007/s00376-014-4192-2.

Rao, J., R. C. Ren, H. S. Chen, Y. Y. Yu, and Y. Zhou, 2018: The stratospheric sudden warming event in February 2018 and its prediction by a climate system model. *J. Geophys. Res.*, **123**(23), 13332−13345, https://doi.org/10.1029/2018jd028908.

Rao, J., R. C. Ren, H. S. Chen, X. W. Liu, Y. Y. Yu, and Y. Yang, 2019: Sub-seasonal to seasonal hindcasts of stratospheric sudden warming by BCC_CSM1.1(m): A comparison with ECMWF. *Adv. Atmos. Sci.*, **36**(5), 479−494, https://doi.org/10.1007/s00376-018-8165-8.

Rao, J., C. I. Garfinkel, and I. P. White, 2020a: Predicting the downward and surface influence of the February 2018 and January 2019 sudden stratospheric warming events in subseasonal to seasonal (S2S) models. *J. Geophys. Res.*, **125**(2), e2019JD031919, https://doi.org/10.1029/2019jd031919.

Rao, J., C. I. Garfinkel, and I. P. White, 2020b: Impact of the quasi-biennial oscillation on the northern winter stratospheric polar vortex in CMIP5/6 models. *J. Climate*, **33**(11), 4787−4813, https://doi.org/10.1175/jcli-d-19-0663.1.

Rao, J., C. I. Garfinkel, and I. P. White, 2020c: How does the Quasi-Biennial Oscillation affect the boreal winter tropospheric circulation in CMIP5/6 models? *J. Climate*, **33**(20), 8975−8996, https://doi.org/10.1175/jcli-d-20-0024.1.

Rao, J., C. I. Garfinkel, I. P. White, and C. Schwartz, 2020d: The Southern Hemisphere minor sudden stratospheric warming in September 2019 and its predictions in S2S models. *J. Geophys. Res.*, **125**(14), e2020JD032723, https://doi.org/10.1029/2020JD032723.

Ren, R. C., and M. Cai, 2007: Meridional and vertical out-of-phase relationships of temperature anomalies associated with the Northern Annular Mode variability. *Geophys. Res. Lett.*, **34**(7), L07704, https://doi.org/10.1029/2006gl028729.

Seviour, W. J. M., D. M. Mitchell, and L. J. Gray, 2013: A prac-

tical method to identify displaced and split stratospheric polar vortex events. *Geophys. Res. Lett.*, **40**(19), 5268−5273, https://doi.org/10.1002/grl.50927.

Seviour, W. J. M., L. J. Gray, and D. M. Mitchell, 2016: Stratospheric polar vortex splits and displacements in the high-top CMIP5 climate models. *J. Geophys. Res.*, **121**(4), 1400−1413, https://doi.org/10.1002/2015jd024178.

Shen, X. C., L. Wang, and S. Osprey, 2020a: The Southern Hemisphere sudden stratospheric warming of September 2019. *Science Bulletin*, **65**(21), 1800−1802, https://doi.org/10.1016/j.scib.2020.06.028.

Shen, X. C., L. Wang, and S. Osprey, 2020b: Tropospheric forcing of the 2019 Antarctic sudden stratospheric warming. *Geophys. Res. Lett.*, **47**, e2020GL089343, https://doi.org/10.1029/2020GL089343.

Sigmond, M., J. F. Scinocca, V. V. Kharin, and T. G. Shepherd, 2013: Enhanced seasonal forecast skill following stratospheric sudden warmings. *Nat. Geosci.*, **6**(2), 98−102, https://doi.org/10.1038/ngeo1698.

Taguchi, M., 2020: Verification of subseasonal-to-seasonal forecasts for major stratospheric sudden warmings in northern winter from 1998/99 to 2012/13. *Adv. Atmos. Sci.*, **37**(3), 250−258, https://doi.org/10.1007/s00376-019-9195-6.

Tripathi, O. P., and Coauthors, 2015: The predictability of the extratropical stratosphere on monthly time-scales and its impact on the skill of tropospheric forecasts. *Quart. J. Roy. Meteor. Soc.*, **141**(689), 987−1003, https://doi.org/10.1002/qj.2432.

Tripathi, O. P., and Coauthors, 2016: Examining the predictability of the stratospheric sudden warming of January 2013 using multiple NWP systems. *Mon. Wea. Rev.*, **144**(5), 1935−1960, https://doi.org/10.1175/mwr-d-15-0010.1.

Wallace, J. M., and D. S. Gutzler, 1981: Teleconnections in the geopotential height field during the Northern Hemisphere winter. *Mon. Wea. Rev.*, **109**(4), 784−812, https://doi.org/10.1175/1520-0493(1981)109<0784:titghf>2.0.co;2.

Wang, L., and W. Chen, 2010: Downward Arctic Oscillation signal associated with moderate weak stratospheric polar vortex and the cold December 2009. *Geophys. Res. Lett.*, **37**, L09707, https://doi.org/10.1029/2010gl042659.

Wei, K., Z. L. Cai, W. Chen, and L. Y. Xu, 2018: The effect of a well-resolved stratosphere on East Asian winter climate. *Climate Dyn.*, **51**(11−12), 4015−4028, https://doi.org/10.1007/s00382-016-3419-6.

White, I., C. I. Garfinkel, E. P. Gerber, M. Jucker, V. Aquila, and L. D. Oman, 2019: The downward influence of sudden stratospheric warmings: Association with tropospheric precursors. *J. Climate*, **32**(1), 85−108, https://doi.org/10.1175/jcli-d-18-0053.1.

Wu, T. W., and Coauthors, 2019: The Beijing Climate Center Climate System Model (BCC-CSM): The main progress from CMIP5 to CMIP6. *Geoscientific Model Development*, **12**(4), 1573−1600, https://doi.org/10.5194/gmd-12-1573-2019.

Yu, Y. Y., M. Cai, R. C. Ren, and J. Rao, 2018: A closer look at the relationships between meridional mass circulation pulses in the stratosphere and cold air outbreak patterns in northern hemispheric winter. *Climate Dyn.*, **51**(7−8), 3125−3143, https://doi.org/10.1007/s00382-018-4069-7.

Zhang, R. H., W. S. Tian, J. K. Zhang, J. L. Huang, F. Xie, and M. Xu, 2019: The corresponding tropospheric environments during downward-extending and nondownward-extending events of stratospheric Northern Annular Mode anomalies. *J. Climate*, **32**(6), 1857−1873, https://doi.org/10.1175/jcli-d-18-0574.1.

Zhou, T. J., and Coauthors, 2020: Development of climate and earth system models in China: Past achievements and new CMIP6 results. *Journal of Meteorological Research*, **34**(1), 1−19, https://doi.org/10.1007/s13351-020-9164-0.